IEEE Access
Multidisciplinary ⋮ Rapid Review ⋮ Open Access Journal

Received July 16, 2021, accepted August 1, 2021, date of publication August 16, 2021, date of current version August 24, 2021.

Digital Object Identifier 10.1109/ACCESS.2021.3104859

PMSM Current Shaping for Minimum Joule Losses While Reducing Torque Ripple and Vibrations

SEBASTIAN CICEO[1,2,3], (Graduate Student Member, IEEE), FABIEN CHAUVICOURT[1], JOHAN GYSELINCK[2], (Member, IEEE), AND CLAUDIA MARTIS[3], (Senior Member, IEEE)

[1]Engineering Consulting Services RTD, Siemens Industry Software NV, 3001 Leuven, Belgium
[2]Electrical Energy Group, Bio, Electro and Mechanical Systems (BEAMS) Department, Université Libre de Bruxelles, 1050 Brussels, Belgium
[3]Department of Electrical Machines and Drives, Technical University of Cluj-Napoca, 400114 Cluj-Napoca, Romania

Corresponding author: Sebastian Ciceo (sebastian.ciceo@mae.utcluj.ro)

This work was supported by the European Industrial Doctorate on Next Generation for sustaINable auTomotive ElectRical ACtuaTion (INTERACT) Project through the European Union Horizon 2020 Research and Innovation Program under Grant 766180.

ABSTRACT This paper presents a current shaping method for torque ripple and mean air-gap radial force-shape harmonics reduction, under minimum Joule losses, used for air-born and structure-born vibration reduction in 3-phase PMSM electric drives. The main source for structure-born noise in electric powertrains is the torque ripple, while the main source for air-born noise are the radial air-gap forces. The proposed method uses a Fourier-decomposed LUT model obtained from updating the 2D electromagnetic FE model using test-bench results. Modal testing is used to update the structural model, and the vibration response on the machine full RPM range is determined using the vibration-synthesis method. The proposed current shaping algorithm is deterministic and can be used on any topology of 3-phase PMSMs. The torque and mean air-gap force harmonics that are intended for reduction can be arbitrary selected and their minimization can be fully completed if the maximum current and voltage constraint are respected. On the machine under test, vibration reduction is accomplished, especially for the mechanical orders that interact with the second mode-shape.

INDEX TERMS Current shaping, MTPA, NVH, optimal control, PMSM, radial force control, torque ripple control.

I. INTRODUCTION

The rapid advancement in automotive electrification requires higher standards for Noise and Vibration (NVH) target setting and thus development of new methods for vibration mitigation. These can be categorized as either early-design stage methods, where the design space is ample, represented by machine cross-section optimization [1], [2], or late-design stage methods where few modifications can be made. For the latter, NVH improvements can be either achieved through machine design methods [3], where small modification, such as rotor notching are made to the cross-section in order to shape the air-gap forces, or control methods where different pulse width modulation (PWM) techniques are adopted [4] or harmonic current control is performed.

On the current control side, it is possible to group by the desired minimization target: torque ripple, air-gap forces or both. Current shaping methods that minimizes the torque ripple under minimum Joule losses exists [5], while online, model-based torque ripple minimization strategies under Maximum-Torque-Per-Ampere (MTPA) conditions are also employed [6], by using genetic algorithms and an analytical PMSM torque ripple model for finding the optimal magnitude and phase for the 6^{th} and 12^{th} dq-current harmonics that represent the set-points to the Proportional-Resonant controllers, [7], [8] that can also include machine temperature variation [9]. In the case of Switched Reluctance Motors (SRMs) the optimal current commutation control problem is solved offline via a optimization routine for the switching-on and switching-off angles [10]. For the air-gap force control, methods based on an analytical models of the air-gap B-field in function of fundamental direct/quadrature (dq) currents [11] together with FE Finite-Element (FE)-correlated analytical force models exists [12]. In [13] the authors propose a method of reducing the vibration response caused by specific radial force-shapes by using a sensitivity analysis on the 6^{th} dq-current harmonic in the electromagnetic FE simulation environment at different speed values. The resulting

The associate editor coordinating the review of this manuscript and approving it for publication was Kan Liu.

forces are exported to the structural-dynamics FE model for vibration computation. Optimization of different current profiles having different harmonics for air-gap force reduction is adopted in [14], while a compensation strategy for radial and tangential forces based on a measured transfer function model (harmonic currents/vibration displacement) is used in [15]. A dynamic programming optimization algorithm that relies on a saturated and rotor position-dependent FE model that minimizes the torque and radial force harmonics simultaneously by harmonic current injection is adopted in [16], while a coupled electromagnetic and structural-dynamics Permanent Magnet Synchronous Machine (PMSM) simulation tool-chain is used to achieved the same desired objective [17].

This paper proposes a new current shaping method that calculates optimal current set-points references to reduce the ripple in the torque and mean air-gap radial force (referred as DC force-shape further on) and Joule losses simultaneously. The DC-force shape harmonics reduction is important because they interact with the stator breathing mode-shape. The method works across the whole machine torque-speed envelope, leading to significant NVH improvements. It is based on Look-Up Tables (LUTs) obtained either from a pure electromagnetic FEA (Finite Element Analysis) or test-correlated FEA. The NVH benefits obtained are important because both structure-born noise caused by the torque ripple and air-born noise caused by the air-gap forces are reduced at the same time. The novelty of the method relies on the deterministic nature, the flexibility of the desired mitigated harmonics and on the fact that it can be universally applied to any PMSM having a 3-phase winding system.

The paper structure follows the diagram in Figure 1. In Section II the machine under study is presented and the procedures used to update the electromagnetic model using back-Electromotive Force (EMF) by changing the Permanent-Magnet (PM) remanence is discussed. Section III presents the harmonics LUT-based machine model (after the updating procedure is applied) that is used in Section IV, where the proposed current shaping algorithm is discussed. The effectiveness of the proposed algorithm on the vibration characteristics is tested numerically using the vibration-synthesis method [18] presented in Section V, where modal testing data is used to correlate the structural model material properties via an optimization routine. Results for the machine full speed range are presented in Section VI, where the added vibration improvements are better accounted for by using the updated structural model.

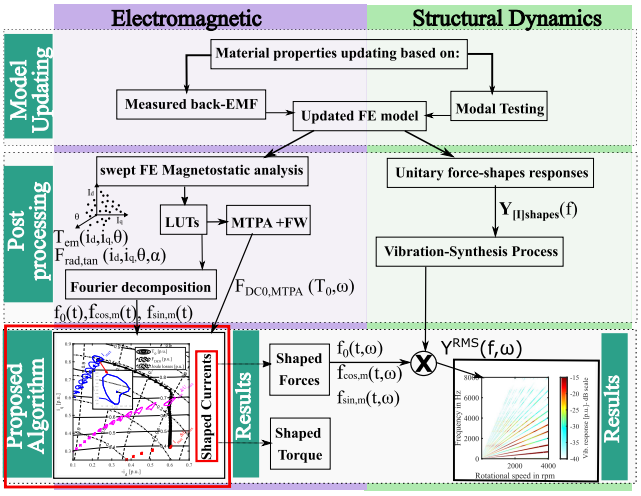

FIGURE 1. Current shaping algorithm: design and testing diagram.

II. ELECTROMAGNETIC MODEL CORRELATION USING TEST RESULTS

A. MACHINE UNDER STUDY

The machine under study is a 12/10 (12 stator teeth and 10 poles) Interior Permanent Magnet Synchronous Machine (IPMSM) with concentrated winding used in electric power steering applications with the specifications given in Table 1 and cross-section in Figure 2.

TABLE 1. IPMSM parameters.

Rated power	800 W
Base speed	1650 RPM
Maximum speed	4000 RPM
Rated current	110 A (rms)
DC-link voltage	12 V
Minimum air-gap	0.5 mm
Stack length	58 mm

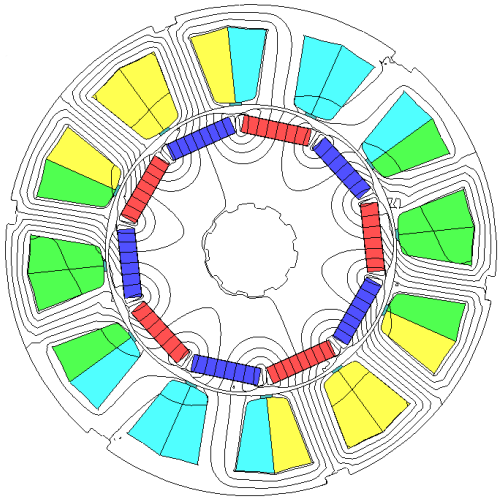

FIGURE 2. Machine cross-section with flux lines at maximum i_q current and $i_d = 0$.

B. ELECTROMAGNETIC FE MODEL CORRELATION

A test-bench consisting of two identical machines coupled at the shaft (Figure 3(a)) is used to measure back-EMF in order to fit the results of the 2-Dimensional (2D) FE model. One parameter is changed in order to match the amplitude of

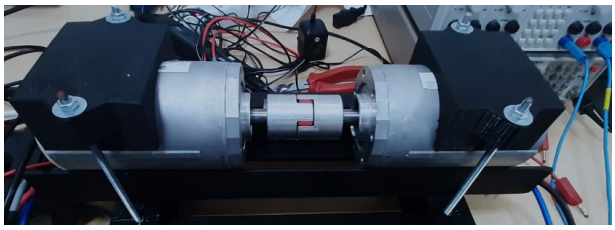

(a) Electric motor test-bench.

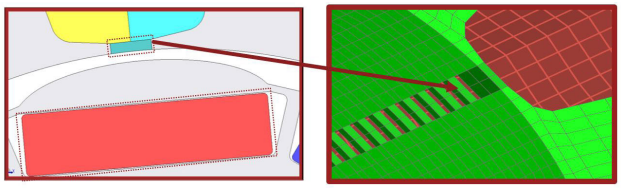

(b) 2D electromagnetic (left) and 3D strucural (right) modelling of the slot openning laminations.

FIGURE 3. PM material model updating using measured back-EMF.

the measured phase voltage at 1000 rpm. The PM remanent flux density (B_r) for the Neodymium-iron-boron (NdFeB) magnet material is changed using a correction factor (ΔB_r) that accounts for 3-Dimensional (3D) effects, such as PM overhang, as shown in [19]. The B-H linear curve for the PM magnetic material is modeled in the second quadrant, where $H_c' = (-B_r + \Delta B_r)/\mu_0\mu_{\text{rec}}$ is the coercive field, μ_0 is the vacuum permeability, μ_{rec} is the relative recoil permeability and $B/B_r = 1 - H/H_c'$. The slot opening (Figure 3(b)) material has the same electric steel material properties as the stator (M800-50A), scaled down with a factor of 3 on the y-axis of the B-H curve. This accounts for the stator modular design - separated tooth segment. The back-EMF result for the correlated model is presented in Figure 4. The model updating procedure is important because the accuracy of the proposed algorithm relies on the accuracy of the electromagnetic model.

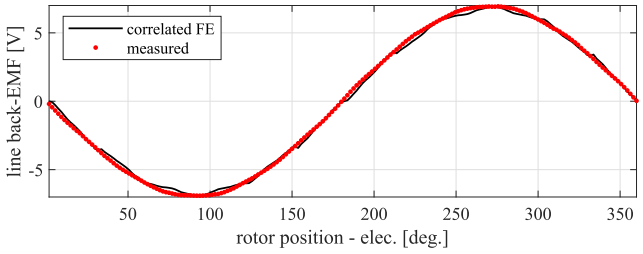

FIGURE 4. Back-EMF comparison between measured and correlated FE model at 1000 RPM.

III. LOOK-UP TABLE BASED NONLINEAR PMSM MODEL

In order to simulate system-level behavior of PMSMs, high-fidelity reduced-order models [20] are needed that include saturation, cross-saturation and slotting effect. A series of magnetostatic FEA that sweep through the current (i_{dq}) and rotor position (θ_m) range are performed and the resulting electromagnetic torque (T_{em}), flux-linkages (λ_{dq}) and air-gap forces ($F_{\text{rad/tan}}$) are post-processed and stored in LUTs as shown in [21].

For a 3-phase machine without homopolar current, the LUTs are either 3D with dq current and rotor position dependency (i_d, i_q, θ_e), in the case of the electromagnetic torque and flux-linkages or 4-Dimensional (4D) - adding the air-gap position dependency ($i_d, i_q, \theta_e, \alpha$) in the case of the air-gap force, where α represents the position along the air-gap.

A. FOURIER-DECOMPOSED PMSM NONLINEAR MODEL

In order to get a better understanding of the harmonic content and reduce the size of the model, a further dimensionality reduction is applied. Specifically, the time dependency in the case of torque and air-gap force is eliminated from the LUT together with α (in the case of the force). This can be achieved by decomposing the variables stored in the LUTs into Fourier series using the cosine and sine coefficients. The variables of interest for the current shaping calculation are the electromagnetic torque (Eq. 1) - decomposed into time harmonics and the air-gap force (Eq. 2) - decomposed into space and time harmonics using the 2D Fourier transform:

$$\begin{aligned} T_{\text{sup}}(t) &= \sum_{n=0}^{N} T_n(t) = T_0(t) \\ &\quad + \sum_{n=1}^{N} (T_{\cos,\text{n}} \cdot \cos(nt) + T_{\sin,\text{n}} \cdot \sin(nt)) \text{ and} \end{aligned} \tag{1}$$

$$\begin{aligned} F_{\text{sup}}(t,\alpha) &= \sum_{m=0}^{M} F_m(t,\alpha) = F_{\text{DC}}(t) \\ &\quad + \sum_{m=1}^{M} (F_{\cos,\text{n}}(t) \cdot \cos(m\alpha) + F_{\sin,\text{n}}(t) \cdot \sin(m\alpha)), \end{aligned} \tag{2}$$

where T_{sup} is the superposed torque waveform that includes all time-dependent harmonic amplitude factors (T_0, $T_{\sin,\text{n}}$, $T_{\cos,\text{n}}$) until the maximum truncated N order and F_{sup} is the 2D superposed air-gap force-wave that contains all space-dependent harmonic amplitude factors (F_{DC} and $F_{\sin,\text{n}}$, $F_{\text{con,n}}$) up to order M.

Additionally, the resulting DC force-shape (F_{DC}) is again decomposed into time-dependent harmonic amplitude factors ($F_{\text{DC},0}, F_{\text{DCsin,n}}, F_{\text{DCcos,n}}$) as in the torque case (Eq. 3), where F_{DCsup} is the superposed DC force-shape that contains all factors up to order N:

$$\begin{aligned} F_{\text{DCsup}}(t) &= \sum_{n=0}^{N} F_{\text{DC,n}}(t) = F_{\text{DC0}}(t) \\ &\quad + \sum_{n=1}^{P} (F_{\text{DCcos,n}} \cdot \cos(nt) + F_{\text{DCsin,n}} \cdot \sin(nt)), \end{aligned} \tag{3}$$

Figure 5 shows the torque and radial DC force-shape dependency measured in per-unit (p.u.) system, where the base unit represents the maximum value of each quantity with respect to i_d, i_q (again, measured in p.u.) and the electrical rotor position θ_e. It can be noticed that higher torque ripple appear in the flux-weakening region (after the base speed) while higher force ripple appear in the maximum torque region.

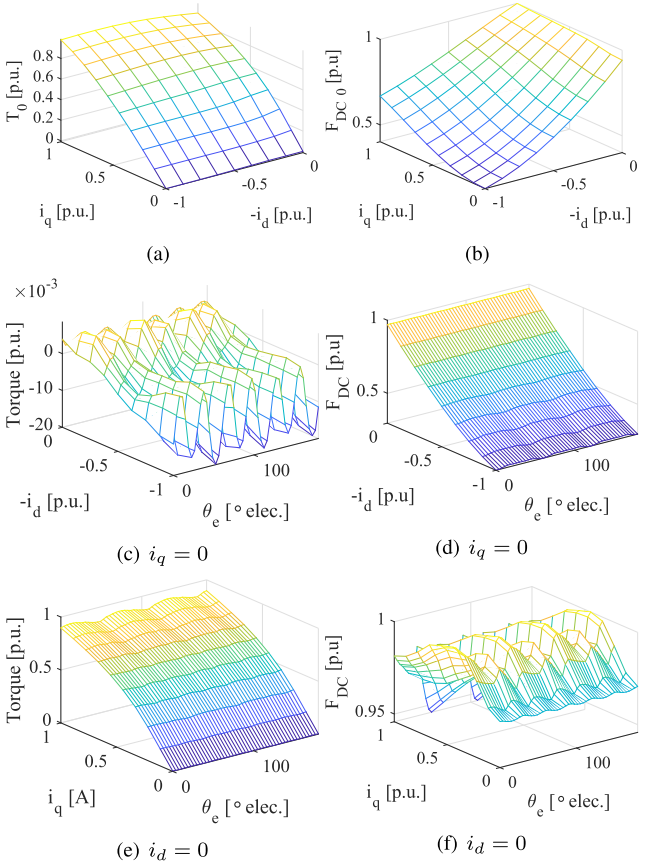

FIGURE 5. Torque and DC force-shape position current and position dependency.

A further reduction in the model size is achieved by truncating the harmonic content of the torque (Eq. 4) and DC force-shape (Eq. 5) wave by using the most significant harmonics in the dq frame, in this case the 0, 6$^{\text{th}}$ and 12$^{\text{th}}$ dq-frame harmonics, as shown (the time dependency is replaced with θ_e):

$$\begin{aligned} &T_{\text{em}}(i_d, i_q, \theta_e) \\ &\quad = T_0(i_d, i_q) + T_{\text{ripple}}(i_d, i_q, \theta_e) \\ &\quad = T_0(i_d, i_q) + T_{\cos 6}(i_d, i_q)\cos(6\theta_e) + T_{\sin 6}(i_d, i_q)\sin(6\theta_e) \\ &\qquad + T_{\cos 12}(i_d, i_q)\cos(12\theta_e) + T_{\sin 12}(i_d, i_q)\sin(12\,\theta_e), \end{aligned} \tag{4}$$

$$\begin{aligned} &F_{\text{DC}}(i_d, i_q, \theta_e) \\ &\quad = F_{\text{DC0}}(i_d, i_q) + F_{\text{DCripple}}(i_d, i_q, \theta_e) \\ &\quad = F_{\text{DC0}}(i_d, i_q) + F_{\text{DCcos6}}(i_d, i_q)\cos(6\theta_e) \\ &\qquad + F_{\text{DCsin6}}(i_d, i_q)\sin(6\theta_e) + F_{\text{DCcos12}}(i_d, i_q)\cos(12\theta_e) \\ &\qquad + F_{\text{DCsin12}}(i_d, i_q)\sin(12\theta_e), \end{aligned} \tag{5}$$

where the i_{dq} dependent torque Fourier cos − sin orthogonal basis are presented in Figure 6.

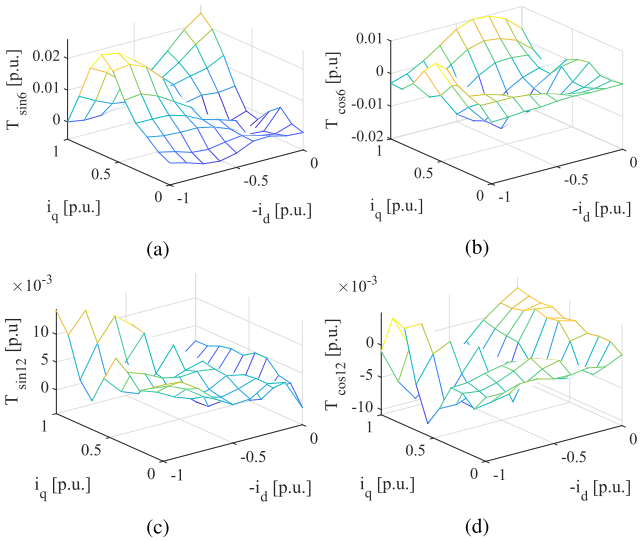

FIGURE 6. Torque harmonic factors: 6$^{\text{th}}$ (a-b) and 12$^{\text{th}}$ (c-d).

The waveform results of the torque and radial DC force-shape for one specific operating point is shown in Figure 7.

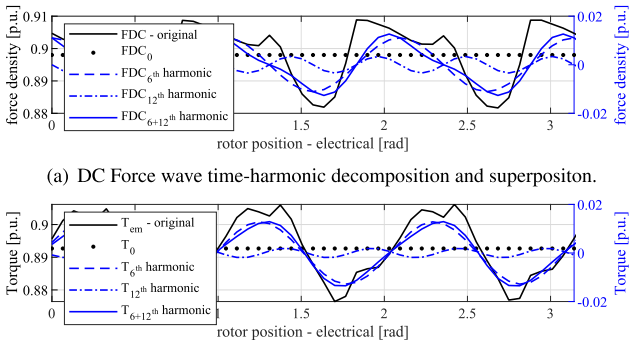

FIGURE 7. Dimensionality reduction via Fourier decomposition for $i_d = 0.25$ p.u. and $i_d = 0.89$ p.u.

IV. OPTIMAL CURRENT SHAPING FOR TORQUE AND DC FORCE-SHAPE RIPPLE CONTROL

In order to minimize the torque and force ripple, the i_{dq} current must be shaped in such a way that it contains counteracting harmonics to the original ripple. The set-points for the mean torque (T_0^*), mean component of the DC force-shape (F_{DC0}^*) and given fixed rotor position (θ_e^*) are considered input to the problem and the optimal currents represent the output. This can be formulated as a system of non-linear equations that are solved for i_d and i_q:

$$\begin{cases} T_0(i_d, i_q) - T_0^* + T_{\text{ripple}}(i_d, i_q, \theta_e^*) = 0 \\ F_{\text{DC0}}(i_d, i_q) - F_{\text{DC0}}^* + F_{\text{ripple}}(i_d, i_q, \theta_e^*) = 0. \end{cases} \tag{6}$$

By solving two equations for each set of dq currents (i_d, i_q) at each rotor position (θ_e^*), the solution is fully determined for a specific set of $(T_0^*, F_{\text{DC0}}^*, \theta_e^*)$. Eq. (6) has the objective of minimizing the torque ripple (T_{ripple}) and radial DC force-shape ripple (F_{DCripple}) concurrently. If the torque ripple is omitted from the formulation, the solution minimizes the DC force ripple only and, vice-versa, if the DC force ripple is omitted the solution minimizes the torque ripple only. Figure 8 shows the harmonic shaped currents for the 3 different optimization scenarios, with the magnitude and phase of the introduced current harmonics resulting from Eq.(6). In this paper only the harmonics shown in Eq.(4) and Eq.(5) are used because the 6^{th} and 12^{th} harmonics are the main contributors to the torque and mean air-gap force ripple. Also, the extension of the algorithm to higher order harmonics, such as the 18^{th} and 24^{th}, would require a higher controller bandwidth in practice, which may lead to implementation issues. It can be noticed that the difference in the wave-shape is caused by the difference in the 6^{th} and 12^{th} current harmonic amplitude, while the DC component remains the same. Figure 9 shows that torque and radial DC force ripple are not fully eliminated because of the existence of higher harmonics that are originally truncated in the problem statement.

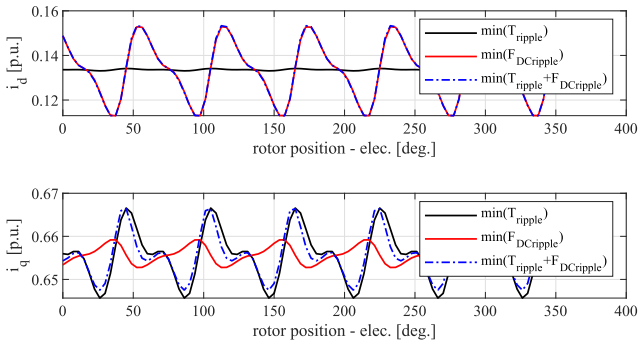

FIGURE 8. Shaped currents for different ripple minimization goals for $T_0^* = 0.738$ [p.u] and $F_{\text{DC0}}^* = 0.907$ [p.u.].

In order to shape the currents on the full torque-speed range, including the flux-weakening (FW) region, for each operating condition (each desired torque set-point and speed), a MTPA optimization is performed where the degrees of freedom (DOF) are again (i_d, i_q) and the resulting mean component of the DC force-shape is stored for each torque and speed set-point $(F_{\text{DC0,MTPA}}(T_0^*, \omega_e^*))$:

$$\begin{cases} \text{minimize Joule losses: } R_s(i_d^2 + i_q^2) \\ \text{equality constraint: } T_0(i_d, i_q) - T_0^* = 0 \\ \text{current limit: } \sqrt{(i_d^2 + i_q^2)} \le I_{\max} \\ \text{voltage limit: } \sqrt{u_d(i_d, i_q, \omega_e^*)^2 + u_q(i_d, i_q, \omega_e^*)^2} \\ \qquad \le U_{\max}, \end{cases} \tag{7}$$

where R_s is the phase resistance, $I_{\max}$ and $U_{\max}$ are the maximum current and voltage values given by the power electronics module, and u_d, u_q are the dq phase voltages.

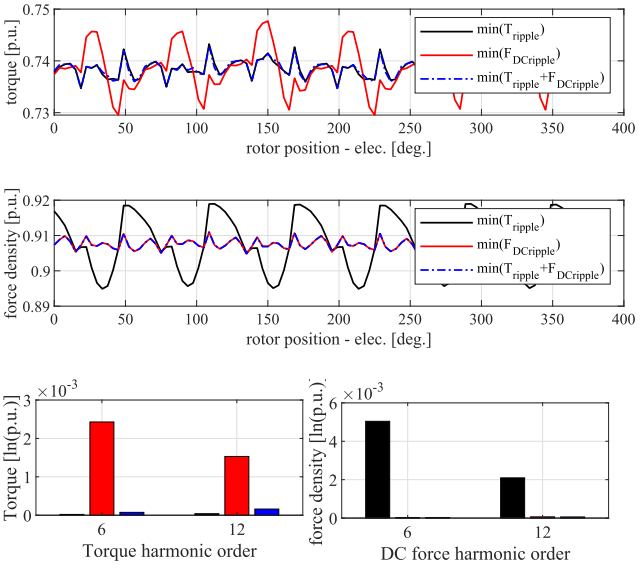

FIGURE 9. Resulting torque and DC force-shape for different ripple minimization goals using the shaped currents showed in Figure 8.

By including the mean component of the DC force-shape obtained from solving the optimization problem $(F_{\text{DC0,MTPA}}(T_0^*, \omega_e^*))$ in Eq.(6), a new system of equations is formed that solves for the dq currents at each rotor position, speed and each mean torque reference:

$$\begin{cases} T_0(i_d, i_q, \omega_e^*) - T_0^* + T_{\text{ripple}}(i_d, i_q, \theta_e^*, \omega_e^*) = 0 \\ F_{\text{DC0}}(i_d, i_q, \omega_e^*) - F_{\text{DC0,MTPA}}(T_0^*, \omega_e^*) + \\ F_{\text{DCripple}}(i_d, i_q, \theta_e^*, \omega_e^*) = 0. \end{cases} \tag{8}$$

The result from solving this equation are a set of dq-currents that are dependent on the DC torque, speed and rotor position: $i_{\text{dq}}(T_0, \omega_e, \theta_e)$. T_0, F_{DC0} and the Joule losses are mapped in Figure 10 using isolines on the i_{dq} range together with the (i_d, i_q) current loci that give the maximum

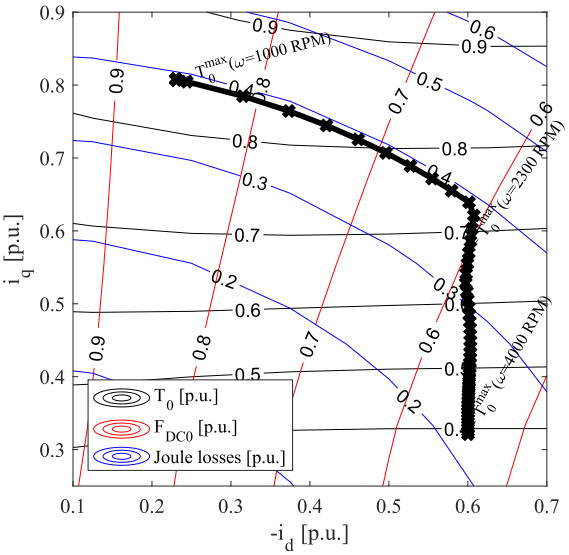

FIGURE 10. Contour plot for T_0 (black), F_{DC0} (red) and Joule losses (blue) on the i_{dq} plane, where the dq-current loci for maximum T_0 under MTPA conditions, at different speed values is marked with black crosses.

T_0 under MTPA conditions, at different speed values (where the p.u. system for the losses is constructed using as base unit the maximum value in the i_{dq} range). It can be remarked that the T_0 isolines are not horizontal due to magnetic saturation and rotor non-salient design and that the maximum T_0 value and the Joule losses are decreasing with the increase in speed after the base speed is reached.

This approach leads to having the same Root-Mean-Square (RMS) Joule losses as in the case of the MTPA control strategy as exemplified in Figure 11. It can be remarked that different i_{dq} orbits obtained from the current shaping algorithm are formed for different reference mean torque and speed values, centered around the value obtained from the MTPA (with flux-weakening) optimization problem.

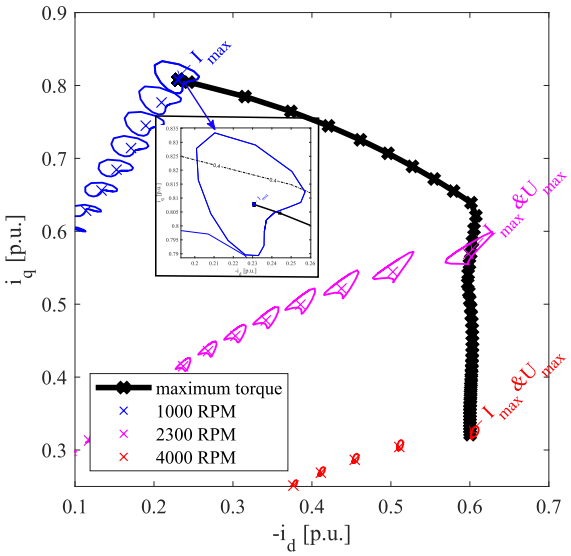

FIGURE 11. Set of (i_d, i_q) current loci for the proposed current shaping algorithm (marked with a solid line) and standard MTPA (marked with crosses) for different speed and torque values and the dq-current loci for maximum T_0, under MTPA conditions, at different speed values is marked with black crosses.

In order to determine the maximum envelope of the torque-speed map, the mean torque is set to be the maximum value for the given speed $i_{dq}^{T_0^{max}}$ ($T_0 = T_0^{max}(\omega_e, \theta_e)$). These currents are shown in Figure 12 representing the i_{dq} speed and rotor position dependent envelope where for each speed, a harmonic current range that center around the values obtained from the standard MTPA (with flux-weakening) is formed. Until the base speed of 1650 RPM the maximum current is the only valid constraint, whereas in the flux-weakening region the voltage limit takes effect.

V. VIBRATION RESPONSE FOR THE FULL TORQUE-RPM RANGE USING THE VIBRATION-SYNTHESIS METHOD

A. STRUCTURAL FE MODEL CORRELATION

Experimental Modal Analysis (EMA) is performed on the machine (with the rotor removed) in order to determine the modal parameters: natural frequencies, mode shapes and modal damping. The test output is the measured

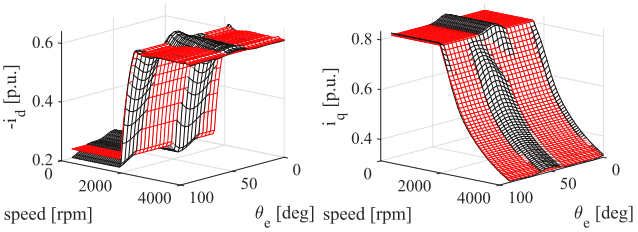

FIGURE 12. Harmonic-shaped (black) and constant (red) dq current values for maximum mean torque across the speed range.

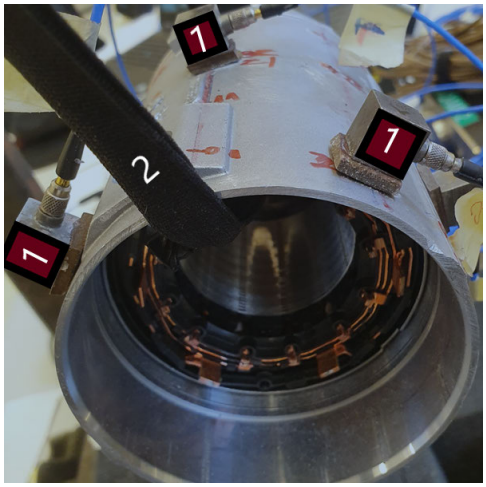

FIGURE 13. EMA test setup where the electric motor with the removed rotor is kept in free-free boundary conditions by the elastic bungee cord (marked with the label 2) and the 3D accelerometers (highlighted in red and marked with label 1) used to measure vibration.

output/input Frequency Response Functions (FRF) - $H_{o/i}$ in free-free boundary conditions. A miniature shaker (LMS Qsource SN045) is used to excite the structure and 36 evenly-distributed triaxial (3D) accelerometers (PCB Piezotronics SN 356A22) placed on the housing's outer surface are used to measure the vibration response. Simcenter SCADAS Lab is used for the data acquisition and the PolyMAX algorithm [22] is used to determine the modal parameters: modal damping ζ_k, residuals A_k and natural frequencies ω_k for each mode k until the maximum truncated mode n, in the desired frequency range (up to 5000Hz) of the linear modal model (where * is the complex conjugate):

$$H_{o/i}(\omega) = \sum_{k=1}^{n} \frac{A_k}{j\omega - \lambda_k} + \frac{A_k^*}{j\omega - \lambda_k^*}, \quad \text{with } \lambda_k = -\zeta_k\omega_k + j\sqrt{1-\zeta_k^2}\omega_k. \tag{9}$$

Using the extracted modal parameters, the anisotropic material properties of the structural FE model (Youngs modulus, shear modulus and the Poisson ratio) are updated in order to match the test results using a optimization routine with the modal frequency difference and the Modal Assurance Criterion (MAC) as correlation metrics [23].

Results from the optimization procedure are presented in Figure 14, where the (a,b) subplots show the deflection for the in-plane ovalization (2,0) and triangle (3,0) mode-shapes obtained with the PolyMax algorithm. The 3D accelerometers placement can also be remarked in the mentioned figures. In the (c,d) subplots the updated FE mode-shapes are shown. It can be noticed that by updating the material properties a relative frequency error below 5% is obtained for each test/simulation mode-shape pair.

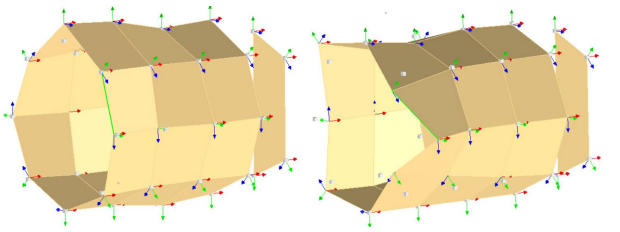

(a) (2,0) at $f = 1192$Hz (test) (b) Mode (3,0) at $f = 2606$Hz (test)

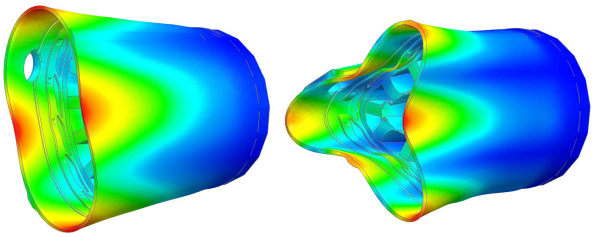

(c) (2,0) at $f = 1265$Hz (simu.) (d) (3,0) at $f = 2674$Hz (simu.)

FIGURE 14. Machine operational deflection shapes (a,b) and correlated FE modal results (c,d).

B. SPATIALLY DECOMPOSED AIR-GAP FORCE

The link between electromagnetic and structural physics computation domain is the radial and tangential air-gap force densities computed using the Maxwell Stress Tensor. $i_{\mathrm{dq}}^{T_0^{\max}}$ is used to interpolate the air-gap B-fields LUTs ($B_{\mathrm{rad,tan}}(i_d, i_q, \theta_m, \alpha)$) obtained in Section III:

$$\begin{aligned} &F_{\mathrm{rad}}(\omega_e, t, \alpha) \\ &\quad = \frac{1}{2\mu_0}\left(B_{\mathrm{rad}}^2\left(i_{\mathrm{dq}}^{T_0^{\max}}(\theta_e, \omega_e), \alpha\right) - B_{\mathrm{tan}}^2\left(i_{\mathrm{dq}}^{T_0^{\max}}(\theta_e, \omega_e), \alpha\right)\right) \\ &F_{\mathrm{tan}}(\omega_e, t, \alpha) \\ &\quad = \frac{1}{\mu_0} B_{\mathrm{rad}}\left(i_{\mathrm{dq}}^{T_0^{\max}}(\theta_e, \omega_e), \alpha\right) B_{\mathrm{tan}}\left(i_{\mathrm{dq}}^{T_0^{\max}}(\theta_e, \omega_e), \alpha\right). \end{aligned} \tag{10}$$

The force is expressed as spatially decomposed superposition of the most important excitation shapes using the $\cos - \sin$ orthogonal basis according to Eq. (2) for each value of the speed, resulting in time and speed dependent amplitude factors $f_{\mathrm{DC}}(\omega_e, t)$, $f_{\cos,\mathrm{m}}(\omega_e, t)$ and $f_{\sin,\mathrm{m}}(\omega_e, t)$ for the maximum torque envelope.

The vibration is calculated as the superposition of dynamic responses excited by each significant force-shape. This is achieved with a modal frequency response solution, having the excitation $F_{[I],\mathrm{shape}}$ a unitary force-shape:

$$v_{[I],\mathrm{shape}}^i(\omega_e, f) = H^i(f) F_{[I],\mathrm{shape}}(\omega_e, f), \tag{11}$$

where $v_{[I],\mathrm{shape}}^i(\omega_e, f)$ is the frequency response in node i for each force-shape excitation, with $H^i(f)$ the output obtained from modal analysis. The total response in node i - $v^i(\omega_e, f)$ is the superposition of all frequency responses scaled with the cos-sin frequency domain amplitude factors:

$$\begin{aligned} &v^i(\omega_e, f) \\ &\quad = v_{[I],\mathrm{DC}}^i(f) f_{DC}(\omega_e, f) \\ &\qquad + \sum_{m=1}^{M}\left(v_{[I],\cos,\mathrm{m}}^i f_{\cos,\mathrm{m}}(\omega_e, f) + v_{[I],\sin,\mathrm{m}}^i f_{\sin,\mathrm{m}}(\omega_e, f)\right), \end{aligned} \tag{12}$$

where the RMS response for all N nodes is:

$$v^{RMS}(\omega_e, f) = \sqrt{\frac{1}{N}\sum_{i=1}^{N} v^i(\omega_e, f)^2}. \tag{13}$$

The structural mesh is shown in Figure 15 where 6 output nodes are selected in order to compute the RMS vibration response.

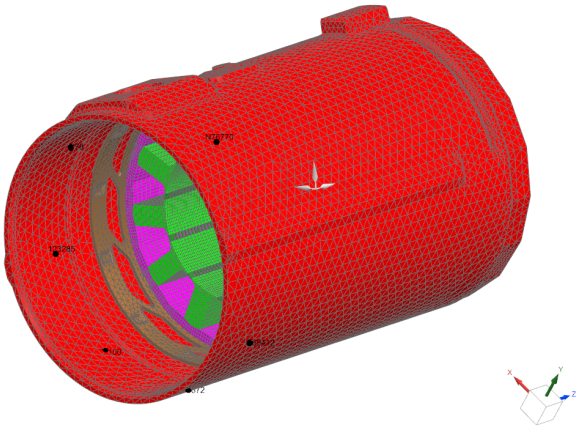

FIGURE 15. Structural mesh with the output vibration computation nodes present on the housing marked in black.

VI. RESULTS

A. TORQUE AND FORCE

Run-up results for the maximum torque and corresponding DC force-shape over the full RPM range are presented in Figure 16. Two results sets, one with the standard MTPA (with flux-weakening) control strategy, and one with the proposed algorithm are shown. It can be observed that both in the case of the torque and DC force-shape the mechanical orders $f = 30 f_{mech}$ and $f = 60 f_{\mathrm{mech}}$ (f_{mech} is the base mechanical frequency) caused by the 6^{th} and 12^{th} dq-current harmonics are completely reduced, with order-cuts shown in Figure 17.

B. VIBRATION RESPONSE

The vibration response is computed using the method described in Section V. The first result set shown in

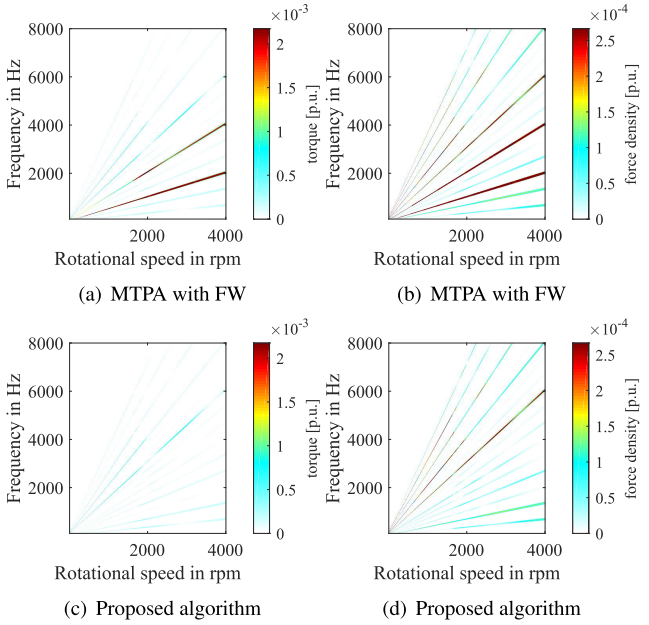

FIGURE 16. Torque and DC force-shape run-up results.

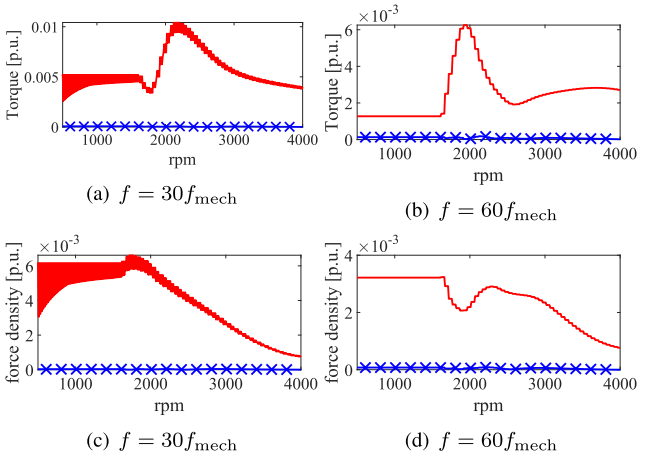

FIGURE 17. Torque and DC force-shape order-cuts for the standard MTPA with flux-weakening (red) and proposed algorithm (blue, with markers): (a,c) - 30th order and (b,d) - 60th order.

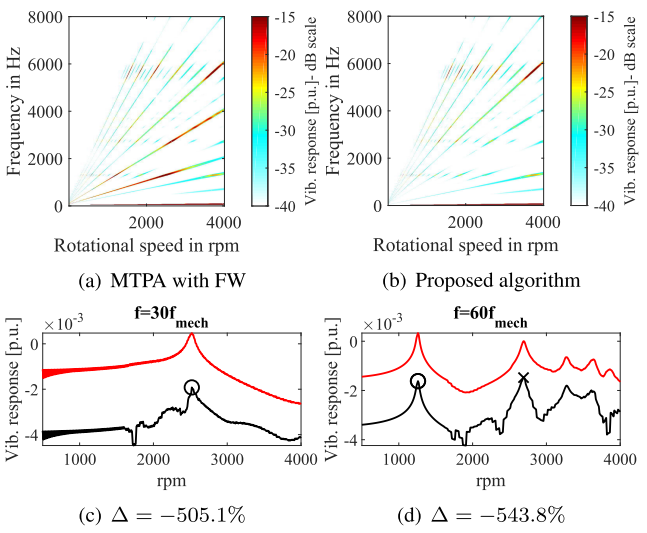

FIGURE 18. Scaled run-up vibration response spectogram (a,b) and order-cuts ((c) - 6th order and (d) - 60th order) using only the DC force-shape, where the MTPA (with flux-weakening) results are represented in (red) and proposed algorithm in (black) and the peak caused by the resonance effect of mode (2,0) is marked with a circle symbol and mode (3,0) with a cross symbol.

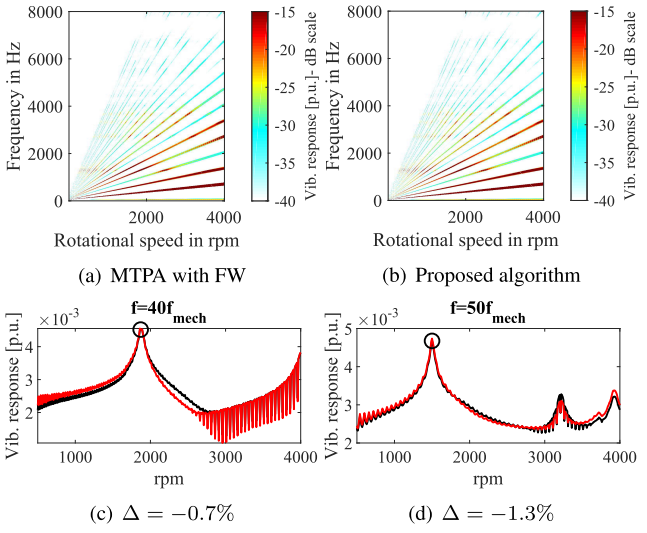

FIGURE 19. Scaled run-up vibration response spectogram (a,b) and order-cuts with the highest vibration-displacement ((c) - 40th order and (d) - 50th order) using all force-shapes, where the MTPA (with flux-weakening) results are represented in (red) and proposed algorithm in (black), where the peak caused by the resonance effect of mode (2,0) is marked with a circle symbol.

Figure 18 represents the vibration displacement for the full RPM-frequency range using just the radial DC force-shape as structural loading ($v_{\text{DC}}^{\text{RMS}}(\omega_e, f)$). This procedure is done in order to compare the effect that the proposed algorithm versus the standard MTPA (with flux-weakening) strategy has on the vibration response. Figure 18 (c,d) represents the mechanical order-cuts and show a significant decrease of order 30 and 60 when using the proposed algorithm, where the relative change in amplitude peak response between the proposed algorithm and the standard MTPA (with flux-weakening) control uses the Δ symbol.

The second result set shown in Figure 19 represents again the vibration displacement for the full RPM-frequency using a number of 40 force-shapes (from the 0 to 40) as structural loading ($v^{\text{RMS}}(\omega_e, f)$). The upper-bound for the force-shape spatial harmonics (40) is limited by Nyquist criterion with the number of nodes along the circumference of the structural mesh. Again, the procedure is adopted for control algorithm comparison and to determine the total effect of radial DC force-shape harmonics reduction on the structural response.

Figure 19 (c,d) represents the mechanical order-cuts for the case where all force-shapes are used to excite the structure, with the first two orders (8 and 10) sorted in terms of the

highest vibration peak shown. The first 10 mechanical orders are quantified in Table 2 in terms of amplitude peak (measured in $10^{-3}p.u.$) and relative peak change Δ. It is observable that the proposed algorithm is beneficial for decreasing 3 out of 4 orders in terms of peak: 40$^{\text{th}}$, 50$^{\text{th}}$ and 70$^{\text{th}}$, where the 20$^{\text{th}}$ order represents the exception.

TABLE 2. Run-up order-cuts peaks.

f	$10f_{mech}$	$20f_{mech}$	$30f_{mech}$	$40f_{mech}$	$50f_{mech}$
peak	47	43	34	45	47
Δ	0%	+2.54%	+1.5%	-0.72%	-1.29%
f	$60f_{mech}$	$70f_{mech}$	$80f_{mech}$	$90f_{mech}$	$100f_{mech}$
peak	24	40	37	21	35
Δ	-8%	-1.38%	+20%	+4.03%	+13.24%

Because the method can be universally applied to 3-phase PMSMs it is reasonable to assume that more significant decrease in vibration response caused by the minimization of DC force-shape harmonics will occur in the case of traction motors. This is explained in [24] where the breathing mode-shape (mode 0) that is excited by harmonics caused by the DC force-shape represents the main source of NVH issues in traction machines.

VII. CONCLUSION

In this paper, a novel current shaping method used in 3-phase PMSMs that reduces the torque and mean radial air-gap force harmonics under MTPA conditions is proposed. The method relies on solving a system of nonlinear equations and uses experimentally-updated Fourier-decomposed LUT models for the machine torque and air-gap force. The method efficiency for PMSM NVH characteristics is validated using a experimentally-updated structural model via the vibration-synthesis. It shows results both in terms of torque ripple reduction, which is the main contributor for the machine structure-born noise, and air-born vibration reduction during run-up operation. If the maximum current and voltage limitation allows, the targeted harmonics in both the torque and mean radial air-gap force can be completely reduced. The consequence of force reduction on the machine vibration characteristics at maximum torque across the whole speed range is a decrease in vibration peaks on the main mechanical orders of 0.72% for the 40$^{\text{th}}$ order and 1.29% for the 50$^{\text{th}}$ order.

As a further investigation, the additional iron losses caused by the harmonic currents should be investigated. Also, the harmonic current injection will be implemented on the test-bench where the practical implementation of harmonic control algorithm, model uncertainty and micro-controller computational speed have to be taken into consideration.

ACKNOWLEDGMENT

Sebastian Ciceo is an Early Stage Researcher in this project. The authors would like to acknowledge JSOL Corporation for granting access to JMAG software packages and Nicolae Zemtev from Siemens Industry Software Brasov for the help provided with the structural modeling.

REFERENCES

[1] A.-C. Pop, J. J. C. Gyselinck, D. E. Pinto, and I. Vintiloiu, "Optimization of low-power brushless PM-machines for automotive applications with focus on high-volume mass production," *IEEE Trans. Ind. Electron.*, vol. 64, no. 12, pp. 9767–9775, Dec. 2017.

[2] I. Ibrahim, R. Silva, M. H. Mohammadi, V. Ghorbanian, and D. A. Lowther, "Surrogate-based acoustic noise prediction of electric motors," *IEEE Trans. Magn.*, vol. 56, no. 2, pp. 1–4, Feb. 2020.

[3] S. Ciceo, F. Chauvicourt, B. Varaticeanu, J. Gyselinck, and C. Martis, "PMASynRM late design-stage rotor shape NVH optimization," in *Proc. Int. Conf. Electr. Mach. (ICEM)*, vol. 1, Aug. 2020, pp. 278–283.

[4] A. Ruiz-Gonzalez, M. J. Meco-Gutierrez, F. Perez-Hidalgo, F. Vargas-Merino, and J. R. Heredia-Larrubia, "Reducing acoustic noise radiated by inverter-fed induction motors controlled by a new PWM strategy," *IEEE Trans. Ind. Electron.*, vol. 57, no. 1, pp. 228–236, Jan. 2010.

[5] G. Bramerdorfer, W. Amrhein, S. M. Winkler, and M. Affenzeller, "Identification of a nonlinear PMSM model using symbolic regression and its application to current optimization scenarios," in *Proc. 40th Annu. Conf. IEEE Ind. Electron. Soc. (IECON)*, Oct. 2014, pp. 628–633.

[6] S. Decker, M. Brodatzki, B. Bachowsky, B. Schmitz-Rode, A. Liske, M. Braun, and M. Hiller, "Predictive trajectory control with online MTPA calculation and minimization of the inner torque ripple for permanent-magnet synchronous machines," *Energies*, vol. 13, no. 20, p. 5327, Oct. 2020.

[7] C. Lai, G. Feng, K. L. V. Iyer, K. Mukherjee, and N. C. Kar, "Genetic algorithm-based current optimization for torque ripple reduction of interior PMSMs," *IEEE Trans. Ind. Appl.*, vol. 53, no. 5, pp. 4493–4503, Sep./Oct. 2017.

[8] C. Lai, G. Feng, K. Mukherjee, V. Loukanov, and N. C. Kar, "Torque ripple minimization for interior PMSM with consideration of magnetic saturation incorporating online parameter identification," *IEEE Trans. Magn.*, vol. 53, no. 6, pp. 1–4, Jun. 2017.

[9] C. Lai, G. Feng, K. Mukherjee, and N. C. Kar, "Investigations of the influence of PMSM parameter variations in optimal stator current design for torque ripple minimization," *IEEE Trans. Energy Convers.*, vol. 32, no. 3, pp. 1052–1062, Sep. 2017.

[10] J. Deskur, T. Pajchrowski, and K. Zawirski, "Optimal control of current switching angles for high-speed SRM drive," *COMPEL Int. J. for Comput. Math. Electr. Electron. Eng.*, vol. 29, no. 1, pp. 156–172, Jan. 2010.

[11] M. Kanematsu, T. Miyajima, T. Enomoto, M. Kondou, H. Komiya, K. Yoshimoto, and T. Miyakawa, "Suppression control of radial force vibration due to fundamental permanent-magnet flux in IPMSM," in *Proc. IEEE Energy Convers. Congr. Expo.*, Sep. 2013, pp. 2821–2826.

[12] T. Hara, S. Aoyagi, T. Ajima, Y. Iwaji, and R. Yoshizu, "Proposal of vibration control reducing 2nd radial electromagnetic force," *Electr. Eng. Jpn.*, vol. 198, no. 1, pp. 45–53, Jan. 2017.

[13] M. Watahiki, T. Mori, L. Lan, J. Tanaka, T. Ueda, T. Fukumura, M. Kanematsu, and H. Fujimoto, "Reduction of sixth-order radial force by harmonic current control and its application to EPS motors," *Electr. Eng. Jpn.*, vol. 209, nos. 3–4, pp. 45–56, Dec. 2019.

[14] J. Krotsch and B. Piepenbreier, "Radial forces in external rotor permanent magnet synchronous motors with non-overlapping windings," *IEEE Trans. Ind. Appl.*, vol. 59, no. 5, pp. 2267–2276, May 2011.

[15] J. Andresen, S. Vip, A. Mertens, and S. Paulus, "Compensation of the radial and circumferential mode 0 vibration of a permanent magnet electric machine based on an experimental characterisation," in *Proc. 22nd Eur. Conf. Power Electron. Appl. (EPE ECCE Europe)*, Sep. 2020, p. 1.

[16] M. Harries, M. Hensgens, and R. W. De Doncker, "Noise reduction via harmonic current injection for concentrated-winding permanent magnet synchronous machines," in *Proc. 21st Int. Conf. Electr. Mach. Syst. (ICEMS)*, Oct. 2018, pp. 1157–1162.

[17] J. Nägelkrämer, A. Heitmann, and N. Parspour, "Application of dynamic programming for active noise reduction of PMSM by reducing torque ripple and radial force harmonics," in *Proc. AEIT Int. Annu. Conf.*, Oct. 2018, pp. 1–6.

[18] M. Boesing, T. Schoenen, K. A. Kasper, and R. W. De Doncker, "Vibration synthesis for electrical machines based on force response superposition," *IEEE Trans. Magn.*, vol. 46, no. 8, pp. 2986–2989, Aug. 2010.

[19] D.-K. Woo, D.-K. Lim, H.-K. Yeo, J.-S. Ro, and H.-K. Jung, "A 2-D finite-element analysis for a permanent magnet synchronous motor taking an overhang effect into consideration," *IEEE Trans. Magn.*, vol. 49, no. 8, pp. 4894–4899, Aug. 2013.
[20] M. Tahkola, J. Keranen, D. Sedov, M. F. Far, and J. Kortelainen, "Surrogate modeling of electrical machine torque using artificial neural networks," *IEEE Access*, vol. 8, pp. 220027–220045, 2020.
[21] S. Ciceo, F. Chauvicourt, J. Gyselinck, and C. Martis, "A comparative study of system-level PMSM models with either current or flux-linkage state variables used for vibro-acoustic computation," in *Proc. IEEE Int. Electric Mach. Drives Conf. (IEMDC)*, May 2019, pp. 1881–1888.
[22] B. Peeters, H. Van der Auweraer, P. Guillaume, and J. Leuridan, "The PolyMAX frequency-domain method: A new standard for modal parameter estimation?" *Shock Vib.*, vol. 11, nos. 3–4, pp. 395–409, 2004.
[23] F. Chauvicourt, C. Faria, J. Gyselinck, and W. Desmet, "Validation of homogenization technique used for accurate predictions of laminated structures mechanical behavior," in *Proc. ISMA Int. Conf. Noise Vibrat. Eng.*, KU Leuven, Belgium, 2016, pp. 1–8.
[24] A. Hofmann, F. Qi, T. Lange, and R. W. De Doncker, "The breathing mode-shape 0: Is it the main acoustic issue in the PMSMs of today's electric vehicles?" in *Proc. 17th Int. Conf. Electr. Mach. Syst. (ICEMS)*, Oct. 2014, pp. 3067–3073.

SEBASTIAN CICEO (Graduate Student Member, IEEE) received the M.Sc. degree in electrical engineering from the Technical University of Cluj-Napoca, in 2017. He is currently pursuing the joint Ph.D. degree with the Université Libre de Bruxelles and the Technical University of Cluj-Napoca. He also works with Siemens PLM Software, Leuven, as an Early-Stage researcher (ESR) in the frame of the H2020 MSCA EID 2017-2021 research project INTERACT. His main research interests include model-based system engineering and testing, electrical machines and drives, electrical mobility, structural dynamics, multibody dynamics, multi-physics optimization and control, and data-driven engineering.

FABIEN CHAUVICOURT received the M.Sc. degree in mechanical engineering from the Université de Technologie de Compiégne, in 2014, and the dual Ph.D. degree in mechanical engineering from the Katholieke Universiteit Leuven, Belgium, and in electrical engineering from the Université Libre de Bruxelles, Belgium, in 2018. He is currently a Research Engineer with Siemens Industry Software NV focusing his research on model-based engineering, such as electric powertrain development, multi-physical system-level modeling, and virtual integration of component behavior, and data-driven engineering, such as artificial intelligence, machine learning, and signal processing.

JOHAN GYSELINCK (Member, IEEE) received the M.Sc. and Ph.D. degrees in electromechanical engineering from Ghent University, Belgium, in 1991 and 2000, respectively. From 2000 to 2004, he was a Postdoctoral Researcher and a Lecturer with the University of Liége, Belgium. Since 2004, he has been a Professor with the Université Libre de Bruxelles (ULB), Belgium. He is the coauthor of some 270 journal and conference papers. His main teaching and research interests include low-frequency numerical magnetics, electrical machines and drives, and renewables, such as wind and photovoltaics.

CLAUDIA MARTIS (Senior Member, IEEE) was born in Macin, Romania, in 1967. She started her university studies, in 1985. She graduated in electrical engineering from Polytechnic Institute, Cluj-Napoca, in 1990, and the Ph.D. degree from the Chair of the Electrical Machines, Marketing and Management, Technical University of Cluj-Napoca, under the coordination of Prof. Karoly-Agoston Biro, in 2001. Her Ph.D. thesis entitled Contributions to the Study of Doubly-Salient Permanent Magnet Reluctance Machines. After three years working as an Engineer with SINTEROM SA, Cluj-Napoca, she joined the Chair of the Electrical Machines, Marketing and Management, Technical University of Cluj-Napoca, first as an Associate Assistant and has been a full-time Teaching and Research Assistant, since 1996. She is currently a Full Professor with the Department of Electrical Machines and Drives, Faculty of Electrical Engineering, Technical University of Cluj-Napoca.